Energy & Environmental Science

ROYAL SOCIETY OF CHEMISTRY

PAPER

View Article Online
View Journal | View Issue

Check for updates

Cite this: *Energy Environ. Sci.*, 2021, **14**, 6616

Ultrafine-grained Ni-rich layered cathode for advanced Li-ion batteries†

Geon-Tae Park,[a] Dae Ro Yoon,[a] Un-Hyuck Kim,[a] Been Namkoong,[a] Junghwa Lee,[b] Melody M. Wang,[b] Andrew C. Lee,[b] X. Wendy Gu,[c] William C. Chueh,[b] Chong S. Yoon*[d] and Yang-Kook Sun*[a]

Received 16th September 2021,
Accepted 15th November 2021

DOI: 10.1039/d1ee02898g

rsc.li/ees

The development of high energy-density Ni-rich (Ni ≥ 90%) layered cathodes has remained difficult because of the rapid capacity fading that occurs during cycling. This study demonstrates that limiting the primary particle size of the cathode resolves the capacity fading problem as nano-sized primary particles effectively relieve the high internal strain associated with the phase transition near charge end and fracture-toughen the cathode. A linear relationship is observed between battery cycling stability and cathode primary particle size. The introduction of Mo inhibits the growth/consolidation of primary particles and limits their size to a submicrometer scale thus improving the cycle life of $Li[Ni_{0.95}Co_{0.04}Mo_{0.01}]O_2$ to a commercially viable level. The $Li[Ni_{0.95}Co_{0.04}Mo_{0.01}]O_2$ cathode, whose microstructure is engineered to mitigate the mechanical instability of Ni-rich layered cathodes, represents a next-generation high energy-density cathode with fast charging capability for electric vehicles with a material cost advantage over current commercial cathodes as Co, a relatively expensive and increasingly scarce resource, is replaced with Ni without compromising battery capacity and battery life.

Broader context

Because the energy-density and cost of Li-ion batteries (LIBs) are largely dictated by their cathode, research has been mostly carried out to improve the performance of the cathode. The Ni-rich layered $Li[Ni_xCo_y(Al \text{ or } Mn)_{1-x-y}]O_2$ (Al = NCA or Mn = NCM) oxide cathodes are the prime candidate cathode materials proposed for the next-generation LIBs. However, the fast capacity fading of Ni-enriched layered cathode which predominantly originates from the build-up of mechanical strain caused by abrupt anisotropic unit cell volume contraction precludes their application in EVs. Here, it was demonstrated that the cycling stability of the NC96 cathode, which is considered to be unsuitable for an application requiring a long battery life, is greatly improved by limiting the primary particle size to an ultrafine scale. The particle size refinement, achieved by inhibiting the grain growth during lithiation through the introduction of a high-valence dopant, gives necessary mechanical toughness and suppresses the nucleation and propagation of microcracks. The NCMo95 cathode whose microstructure is engineered to mitigate the mechanical instability of Ni-rich layered cathodes represents a next-generation high-energy-density cathode with long life and fast charging capability.

Introduction

The high energy-density of Li-ion batteries (LIBs) is the primary reason for the rapid development of LIBs as mainstream rechargeable batteries with a wide range of applications. Unlike lead–acid (30–40 W h kg^{-1}) or Ni–metal-hydride (80 W h kg^{-1}) batteries, state-of-the-art LIBs can provide up to 200 W h kg^{-1}, which is sufficient to power high-end electric vehicles (EVs).[1–3] Although EVs powered by LIBs are rapidly gaining a market share owing to government subsidies and regulations, EVs still cannot compete with internal combustion engine vehicles in terms of cost.[4] In addition, the energy-densities of LIBs are still significantly less than that of gasoline. One of the consequences of the relatively low energy-density of LIBs is that EVs are weighed down by large arrays of batteries, which account for 30–40% of their net weight. Hence, even an incremental increase in the energy-density of LIBs can substantially reduce the EV weight and power demands on the drive system. A higher energy-density also translates to a longer driving

[a] *Department of Energy Engineering, Hanyang University, Seoul 04763, South Korea. E-mail: yksun@hanyang.ac.kr*
[b] *Department of Materials Science and Engineering, Stanford University, Stanford, California 94305, USA*
[c] *Department of Mechanical Engineering, Stanford University, Stanford, California 94305, USA*
[d] *Department of Materials Science and Engineering, Hanyang University, Seoul 04763, South Korea. E-mail: csyoon@hanyang.ac.kr*

† Electronic supplementary information (ESI) available. See DOI: 10.1039/d1ee02898g

Open Access Article. Published on 16 November 2021. Downloaded on 5/26/2026 9:29:26 AM. This article is licensed under a Creative Commons Attribution-NonCommercial 3.0 Unported Licence.

This journal is © The Royal Society of Chemistry 2021

Open Access Article. Published on 16 November 2021. Downloaded on 5/26/2026 9:29:26 AM.
This article is licensed under a Creative Commons Attribution-NonCommercial 3.0 Unported Licence.

range, as more batteries can be installed in an EV. The energy-density and cost of LIBs are largely determined by their cathodes. Layered $Li[Ni_xCo_y(Al\text{ or }Mn)_{1-x-y}]O_2$ (Al = NCA or Mn = NCM) cathodes are archetypal cathodes for the current fleet of EVs. Increasing the energy-density and reducing the cost of these NCA and NCM cathodes requires the replacement of expensive Co with Ni. However, the inherent structural instability of Ni-enriched layered oxide cathodes, particularly in the deeply charged state, leads to a build-up of mechanical strain resulting from the abrupt anisotropic contraction of the unit cell.[5,6] The strain build-up causes the nucleation and propagation of microcracks, which enable electrolyte infiltration and accelerate structural deterioration, which has plagued attempts to stabilize the cycling performance of Ni-rich layered cathodes.[7,8] Therefore, ensuring sufficient cycling stability, and hence, battery life, for Ni-rich layered cathodes essentially requires the dissipation of the strain energy and fracture-toughening of the cathode. To date, approaches proposed to prevent or minimize microcrack formation in Ni-rich NCM and NCA cathodes in the deeply charged state predominantly rely on chemical protection based on coating or modifying cathode surfaces and internal grain boundaries but fail to provide a reliable and cost-effective solution.[9–14]

Decreasing the grain size of structural ceramic materials to ultrafine ($<$ 500 nm) or nanometer scale ($<$ 100 nm) can enhance the mechanical strength and fracture toughness of ceramic materials.[15–17] The grain boundaries in these ultrafine-grained and nanocrystalline ceramics are short and zigzagged owing to numerous triple junctions. Hence, the long and tortuous paths that intergranular cracks must follow along the grain boundaries deter their propagation.[18] The same mechanism can be used to fracture-toughen delithiated Ni-rich layered cathodes. However, preparing an ultrafine-grained cathode is not a trivial matter. The conventional method for synthesizing Ni-rich layered cathodes involves the preparation of a hydroxide precursor using co-precipitation that which is subsequently lithiated at a high-temperature (at $>$ 700 °C). The hydroxide precursor consists of nano-sized particles loosely held in a spherical secondary particle. During lithiation, these loosely held primary particles consolidate and invariably coarsen such that the size of the final primary particles of $Li[Ni_{0.80}Co_{0.15}Al_{0.05}]O_2$, a popular commercial cathode, routinely exceeds 500 nm.[19–21] To inhibit such particle coarsening, ultrafine or nanoceramic materials are usually sintered under non-equilibrium conditions, requiring specialized processes, such as spark plasma sintering, which are not applicable for cathode powders.[22] One cost-effective way of inhibiting particle coarsening is the modification of grain boundaries with dopants, which can retard the diffusion of matrix atoms. Dopants with limited solubility are preferred because excess dopant atoms tend to segregate at interparticle boundaries and impede the migration of matrix atoms across the grain boundaries. Recent reports of W-doped layered cathodes suggest that significantly smaller primary particles can be produced by introducing excess dopant into the layered structure.[23,24] In this work, to limit the primary particle size to well below 500 nm without resorting to specialized processing techniques, a series of dopants were introduced into $Li[Ni_{0.96}Co_{0.04}]O_2$ (NC96). Some dopants were found to be more effective than others in limiting the primary particle size, enabling the explicit examination of the effect of primary particle size on the cycling stability of the cathode. Of the studied dopants, Mo achieved the largest refinement effect. Mo-doping of NC96, whose severe capacity fading precludes its use in long-term applications such as EVs, produces ductile mechanical behavior and improves battery life to a commercially viable level despite the high Ni content.

Results and discussion

Among the various Al-, Mn-, Ti-, Ta-, Sb-, Nb-, W-, and Mo-doped cathode materials, the Mo-doped cathode material ($Li[Ni_{0.95}Co_{0.04}Mo_{0.01}]O_2$, NCMo95) exhibits the most pronounced size refinement effect, as the width of its primary particles is well below 500 nm even when lithiated at 800 °C, which is much higher than the optimal lithiation temperature (Fig. 1a). An Al-doped cathode material ($Li[Ni_{0.95}Co_{0.04}Al_{0.01}]O_2$, NCA95), which belongs to the well-characterized NCA family, is used as a performance benchmark. When NCMo95 and NCA95, derived from identical hydroxide precursors with an average primary particle size of ~70 nm, are lithiated at 700, 750, and 800 °C, the size of the primary particles of NCA95 greatly increases in width from 560 nm to $>$ 1 μm, while that of the primary particles of NCMo95 is virtually unchanged (Fig. S1, ESI†). To investigate the different coarsening behaviors of the cathode particles, NCA95 and NCMo95 cathodes were lithiated at 700 °C for different durations (see Table S1 for their chemical compositions determined by inductively coupled plasma optical emission spectroscopy (ICP-OES), ESI†). The average NCA95 primary particle size of 560 nm after a lithiation time of 10 h increases to 1207 nm after 60 h (Fig. 1b). In comparison, the average NCMo95 primary particle size increases from 150 to 215 nm with increasing lithiation time from 10 to 60 h (Fig. S2, ESI†). Changes in the size and shape of the primary particles of NCA95 and NCMo95 are summarized in Fig. 1c and d, which plot the particle width and aspect ratio (length/width) as a function of lithiation time, respectively. The size and equiaxiality of NCA95 primary particles increase with increasing lithiation time. In contrast, the width of NCMo95 primary particles remains less than 250 nm even after a lithiation time of 60 h as the cathode retains the needle-like primary particles of the hydroxide precursor (Fig. S3, ESI†). ASTAR analysis confirms that strong crystallographic texture is also well preserved in NCMo95 cathodes (Fig. S4, ESI†). To elucidate the growth-inhibiting effect of Mo doping, the average primary particle width was fitted to the following grain growth equation, where D_0, k, t, and n are the initial particle size, rate constant, calcination time, and growth exponent, respectively (Fig. 1e).[25,26]

$$D^n - D_0^n = kt$$

The n obtained for the NCA95 cathode is 2.3, which is close to the value predicted by the theoretical model of Burke and

Open Access Article. Published on 16 November 2021. Downloaded on 5/26/2026 9:29:26 AM.
This article is licensed under a Creative Commons Attribution-NonCommercial 3.0 Unported Licence.

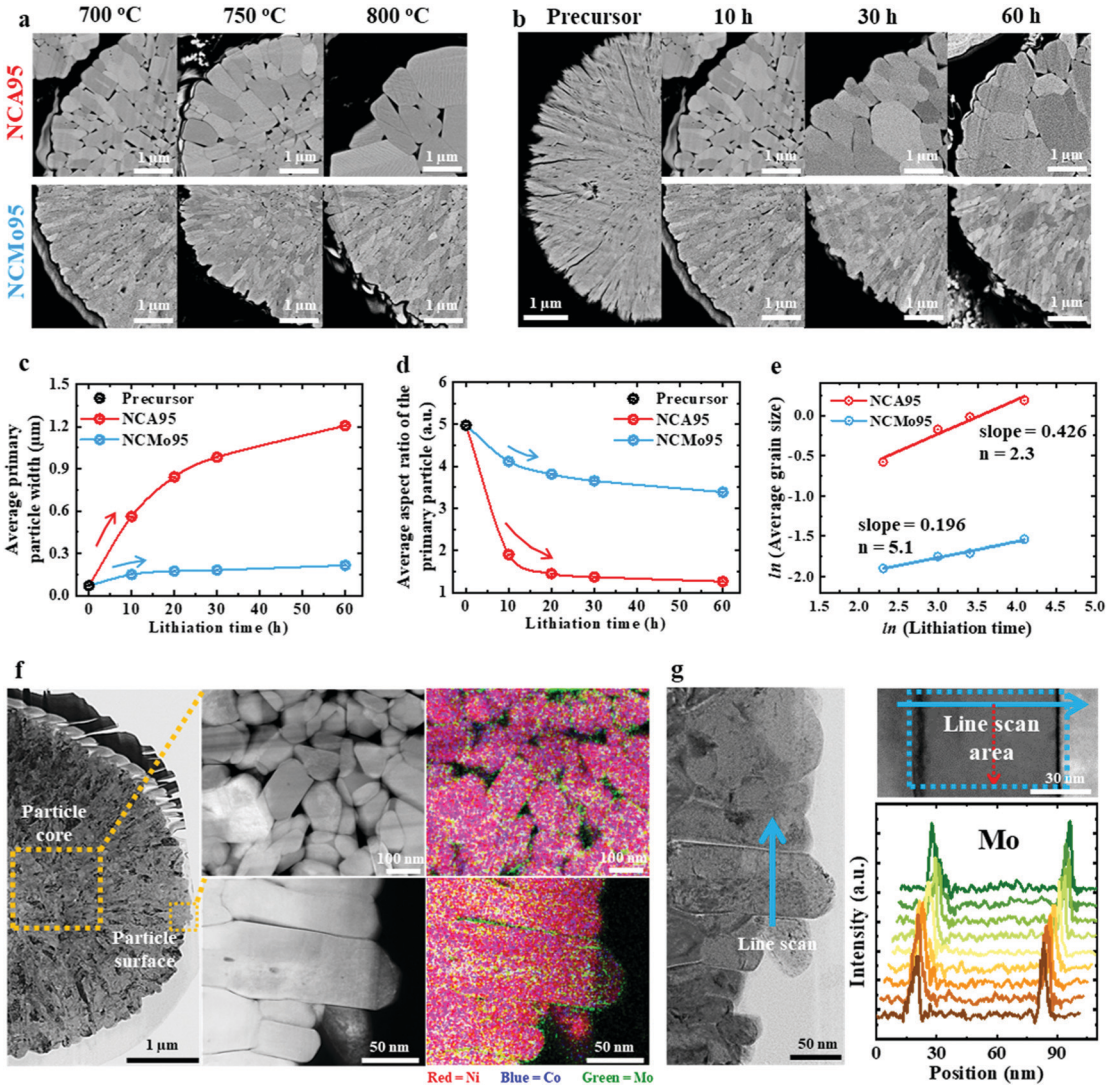

Fig. 1 Particle morphology under various lithiation conditions and distribution of transition metal elements. Cross-sectional SEM images of a $[Ni_{0.96}Co_{0.04}](OH)_2$ precursor, NCA95, and NCMo95 cathode particles (a) lithiated at 700, 750, and 800 °C for 10 h and (b) lithiated at 700 °C for 10, 30, and 60 h. (c) Average primary particle width and (d) aspect ratio (expressed as length/width) of the hydroxide precursor, NCA95, and NCMo95 cathode particles as functions of lithiation time. (e) Grain growth exponent for NCA95 and NCMo95 cathodes calculated in terms of a grain growth equation. (f) Bright-field cross-sectional STEM images, TEM-EDX elemental maps, and (g) results of a TEM-EDX line scan of an NCMo95 cathode particle lithiated at 700 °C for 10 h.

Turnbull. The model assumes that the grain growth depends solely on the curvature of the particle boundary and that no drag force exists from secondary particles and solutes.[27,28] In contrast, the n obtained for NCMo95 is 5.1, deviating significantly from the theoretical model. This high value of n is indicative of effective particle growth inhibition. Such a high n is also observed in sintered ceramic materials where the migration of grain boundaries is retarded by secondary phases.[29,30] In NCMo95, Mo^{6+} with a higher oxidation valence is likely insoluble in the layered structure, resulting in the accumulation of excess Mo^{6+} along interparticle boundaries where loose local structures can accommodate the difference in the ionic radii and oxidation states. The solute atoms then restrict particle growth, as the grain boundaries are pinned by the solute atoms (Fig. S5, ESI†). Direct evidence of the segregation of Mo was obtained through the elemental mapping of NCMo95 that was lithiated for 10 h at 700 °C using transmission electron microscopy–energy dispersive X-ray (TEM-EDX) analysis (Fig. 1f). Mo atoms are preferentially located along the interparticle boundaries. The segregation of Mo is further evidenced by the elemental line scans across primary particle boundaries, which show that the Mo concentration sharply increases at these boundaries (Fig. 1g). The segregation of Mo along the boundaries persists even after prolonged annealing, *i.e.*, a lithiation time of 60 h (Fig. S6 and S7, ESI†), indicating that Mo effectively inhibits grain growth by segregating along interparticle boundaries and pinning the boundary. Similar to Mo, solute segregation at interparticle

 This journal is © The Royal Society of Chemistry 2021

Open Access Article. Published on 16 November 2021. Downloaded on 5/26/2026 9:29:26 AM.
This article is licensed under a Creative Commons Attribution-NonCommercial 3.0 Unported Licence.

boundaries is observed for other high-valence dopants such as Nb, Sb, and W (Fig. S6 and S7, ESI†).

The introduction of Mo not only affects the particle growth kinetics of the cathode but also subtly alters its crystal structure. The crystal structure of a layer-type cathode increasingly destabilizes during charging as Li ions are removed from the lattice; it is at its most vulnerable state at full charge. The removal of a large fraction of Li ions from the lattice causes an abrupt contraction in the *c*-direction and the resulting strain leads to the eventual mechanical failure of the cathode.[5,31,32] Hence, the stability of the delithiated structure is critical for preserving the crystal structure and minimizing mechanical damage during long-term cycling. NCA95 and NCMo95 cathodes that were lithiated at 700 °C for 10 h were charged to a voltage of 4.5 V, at which 91% of the Li^+ in these cathodes is removed. These delithiated structures were observed by TEM. A SAED pattern recorded along the [100] zone axis of a primary particle of the charged NCA95 cathode displays streaks in the *c*-direction, suggesting narrow regions with stacking faults, and elongated diffraction spots, indicating misaligned Li and transition metal (TM) layers (Fig. 2a). The corresponding HRTEM image shows distorted TM slabs that are curved and disjointed as the intermittent absence of Li ions results in the localized collapse of layer planes (Fig. 2b). Such structural distortion in the deeply charged state impairs the reversible insertion of Li ions into the lattice during discharge, leading to irreversible capacity fading that plagues the cycling stability of Ni-rich NCA and NCM cathodes. The incorporation of Mo into the layered structure produces a highly ordered structure with minimal distortion of the Li and TM layers (Fig. 2c and d). A SAED pattern recorded along the $[1\bar{1}0]$ zone axis of a primary particle of a charged NCMo95 cathode (in Fig. 2c) is free of streaks and its diffraction spots are round and sharply defined. Moreover, the SAED pattern displays forbidden spots when compared with a simulated SAED pattern along the $[1\bar{1}0]$ zone axis. The extra spots indicate the existence of a superlattice in the *a*–*b* plane. A possible explanation of the observed diffraction pattern is the existence of a superlattice unit cell with a periodicity of 2*a* with Li atoms or Ni vacancies in the middle of the unit cell, as shown in Fig. 2e and f. The projection of this superlattice unit cell along the $[1\bar{1}0]$ zone axis produces a row of atoms with a periodicity of 0.28 nm owing to the partial absence of TM ions. In contrast, the normal layered unit cell projected in the same direction generates a row of atoms with a periodicity of 0.14 nm. A TEM image of the region confirms the periodicity of 0.28 nm along the Ni and Li layers. Fig. 2g and h show schematic images of the Li/TM cation-ordered structure and normal layered structure, respectively. Maintaining charge neutrality while retaining Mo^{6+} in the layered structure requires the reduction of Ni^{3+} to Ni^{2+}, whose ionic radius is similar to that of Li^+. This similarity in ionic size facilitates the migration of Ni^{2+} into the Li slab, which is substantiated by the Rietveld refinement of the X-ray diffraction (XRD) data of NCA95 and NCMo95 (Fig. S8 and Tables S2, S3, ESI†). The consequent presence of Ni in the Li slab prevents the local collapse of the layered structure and stabilizes the delithiated structure. The straight and continuous Li and TM slabs in the cation-ordered region clearly attest to the stability of the crystal structure, which improves the cycling stability achieved by the cathode. The cation ordering observed in the deeply charged state is also observed for the pristine NCMo95 cathode (Fig. S9, ESI†), verifying the increased presence of Ni^{2+} ions due to the doping of Mo^{6+} and the subsequent migration of Ni^{2+} ions into the Li slab. The enhanced cycling stability achieved by other layered cathodes, including $Li[Ni_{0.5}Mn_{0.5}]O_2$, Zr-doped $LiNiO_2$, an NCA/NCMA cathode with a core–shell structure, and $Li[Ni_{0.90}Co_{0.09}Ta_{0.01}]$, has been attributed to a cation-ordered structure, similar to that observed in the charged NCMo95 cathode.[33–36] The presence of Ni^{2+} ions in the Li slab prevents the local collapse of the layered structure and preserves the structural framework even in a highly delithiated state, thus improving the reversibility of Li intercalation.

The fundamental electrochemical performances of NCA95 and NCMo95 cathodes lithiated for 10, 30, and 60 h at 700 °C and cycled to 4.3 V in CR2032 coin-type half-cells with Li-metal anodes were compared. The initial charge–discharge curves charged at 0.1 C and 30 °C show that the discharge capacity of the NCA95 cathode decreases from 235 to 233 mA h g^{-1} with increasing lithiation time from 10 to 60 h whereas that of the NCMo95 cathode remains at 242 mA h g^{-1} regardless of lithiation time (Fig. S10, ESI†). While extended lithiation time likely improve the crystallinity of the layered cathode structure and anneals out structural defects, the consolidation/growth of the primary particles substantially undermines the cycling stability of the NCA95 cathode. The cycling data in Fig. 3a indicate that a half-cell cycled at 0.5 C using the NCA95 cathode with an average primary particle width of 560 nm (lithiated for 10 h) retains 80% of its initial capacity after 100 cycles; however, the capacity retention decreases sharply to 69% in the case of the NCA95 cathode with an average primary particle size of 1207 nm (lithiated for 60 h). In comparison, the NCMo95 cathode with an average primary particle size of 150 nm (lithiated for 10 h) exhibits superior cycling stability, retaining 91% of its initial capacity (Fig. 3b). The capacity retention of the NCMo95 cathode subjected to extended lithiation (lithiation time of 60 h) at 87.2% is less than that of its counterpart featuring an NCMo95 cathode lithiated for 10 h, but it is still superior to that of the NCA95 cathode lithiated for 10 h. This is likely because the primary particles of the NCMo95 cathode lithiated for 60 h are still substantially smaller than those of the NCA95 cathode lithiated for 10 h. Half-cells featuring NCA95 and NCMo95 cathodes lithiated at different temperatures reveal a similar cycling stability trend, *i.e.*, cycling stability decreases with increasing primary particles size (Fig. S11, ESI†). Fig. 3c shows the initial discharge capacity and capacity retention of half-cells, featuring NCA95 and NCMo95 cathodes lithiated at 700 °C, after 100 cycles as functions of cathode primary particle width. Particle size is clearly correlated with cycling stability, substantiating that the size refinement of cathode particles facilitates the effective dissipation of the strain in the deeply charged state and fracture-toughens the cathode. The discharge capacity is weakly correlated with primary particle width, suggesting that size refinement does

Open Access Article. Published on 16 November 2021. Downloaded on 5/26/2026 9:29:26 AM.
This article is licensed under a Creative Commons Attribution-NonCommercial 3.0 Unported Licence.

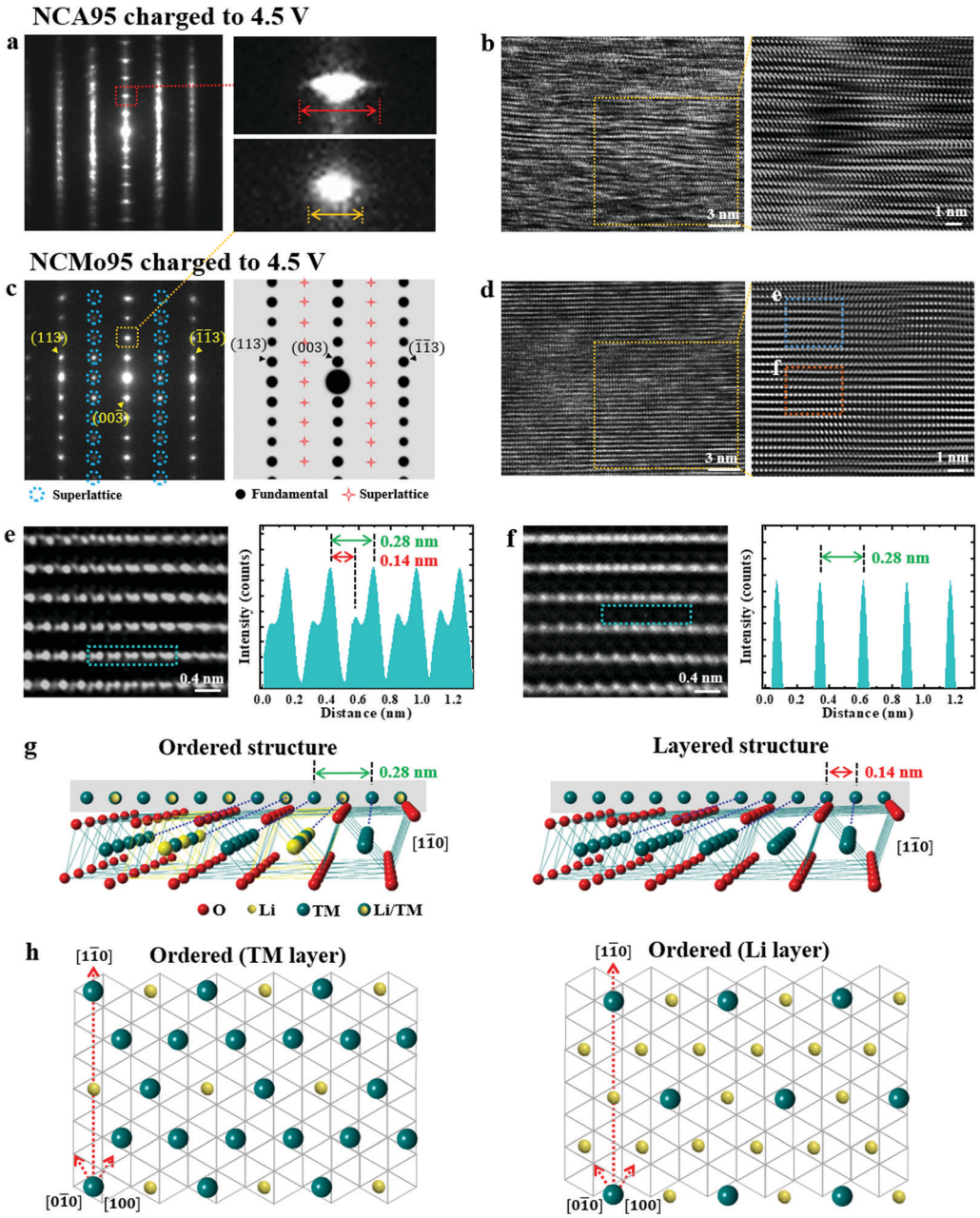

Fig. 2 Structural stability of delithiated NCA95 and NCMo95 cathode particles and Li/TM cation-ordered structure observed in an NCMo95 cathode particle. (a and c) SAED images (left) with simulated diffraction patterns (right) and (b and d) HRTEM images (left) with inverse fast Fourier transform TEM images (right) of delithiated NCA95 and NCMo95 cathode particles, *i.e.*, charged to 4.5 V (superlattice spots distinct from the normal layered structure are marked in blue and red). (e and f) High-angle annular dark-field (HAADF) TEM images of marked regions in (d) (left) with contrast line scans of the Li/TM cation-ordered structure (right) demonstrating the alternating occupation of the structure by Li and TM atoms. (g) Schematic three-dimensional image of the Li/TM cation-ordered structure and normal layered structure. (h) Schematic two-dimensional image of the Li/TM cation-ordered structure with respect to the TM and Li layers viewed along the [1$\bar{1}$0] axis.

not affect the Li-intercalation chemistry. The initial discharge delivered by the NCMo95 cathode is close to 90% of the theoretical capacity, which is equivalent to a cathode energy-density of 895 W h kg^{-1} cathode. This energy-density satisfies the threshold energy-density requirements of EVs. Moreover, the NCMo95 cathode contains substantially less Co (it is replaced with Ni) than current commercial Ni-rich NCA cathodes, $Li[Ni_{0.8}Co_{0.15}Al_{0.05}]O_2$; as a result, owing to the increasing scarcity of Co, the proposed cathode is more sustainable and cost effective. The cycling stability of the NCMo95 cathode was further investigated during long-term cycling in pouch-type full-cells featuring graphite anodes; the cells were charged and discharged at 0.8 and 1.0 C respectively, between 3.0 and 4.2 V (Fig. 3d). The full-cell featuring an NCMo95 cathode (lithiated for 10 h) retains

 This journal is © The Royal Society of Chemistry 2021

Open Access Article. Published on 16 November 2021. Downloaded on 5/26/2026 9:29:26 AM.
This article is licensed under a Creative Commons Attribution-NonCommercial 3.0 Unported Licence.

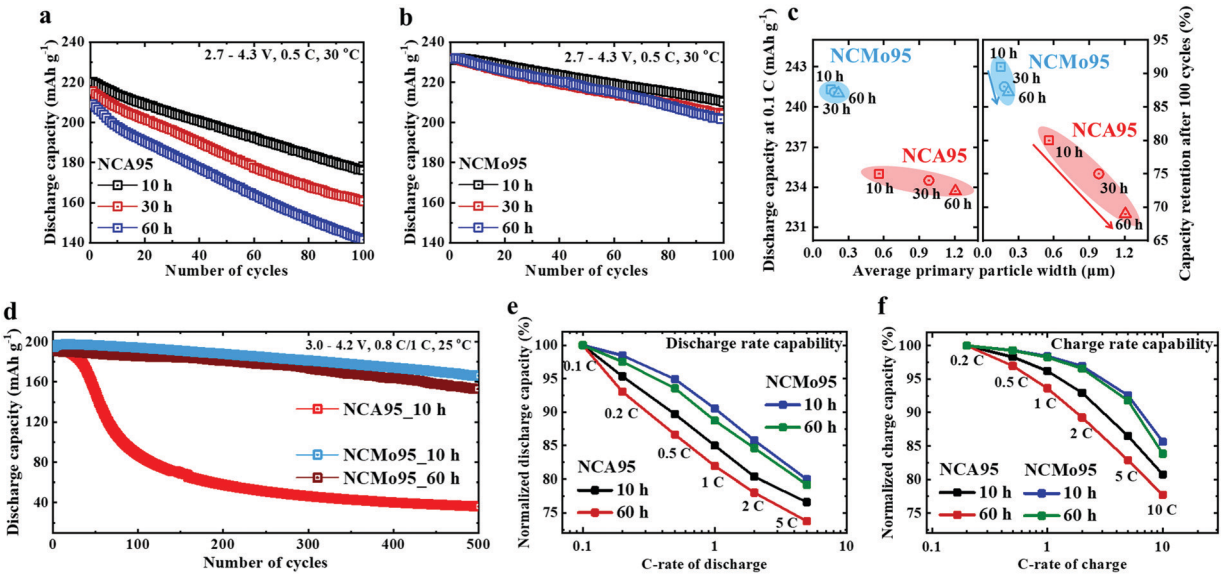

Fig. 3 Electrochemical performances of NCA95 and NCMo95 cathodes lithiated for various lithiation time. Cycling performance (at 0.5 C) achieved by the (a) NCA95 and (b) NCMo95 cathodes lithiated at 700 °C for 10, 30, and 60 h. (c) Discharge capacity (at 0.1 C) and capacity retention after 100 cycles, achieved by NCA95 and NCMo95 cathodes subjected to different lithiation time, as functions of average primary particle width. (d) Comparison of full-cell cycling performances achieved by NCA95 and NCMo95 cathodes subjected to different lithiation time. Comparison of the (e) discharge rate capabilities and (f) charge rate capabilities of cells featuring NCA95 and NCMo95 cathodes subjected to different lithiation time.

85.3% of its initial capacity after 500 cycles while cycling at full depth of discharge. In contrast, the full-cell featuring an NCA95 cathode loses more than 50% of its initial capacity after only 100 cycles. Increasing the primary particle size of the NCMo95 cathode by subjecting it to extended lithiation (lithiation time of 60 h) also deteriorates the cycling stability of the resulting full-cell (it retains 80.2% of its initial capacity after 500 cycles), confirming the correlation between primary particle size and cycling stability. Thus, the particle-size-refined NCMo95 cathode represents a new class of Ni-rich layered cathode that provides both high energy-density and long battery life, suitable for EV application, at a comparatively low material cost. The large fraction of interparticle boundaries in the particle-size-refined NCMo95 cathode also provides fast diffusion pathways, expediting Li^+ migration, and thereby enhancing battery rate capability.[37–39] The NCA95 and NCMo95 cathodes lithiated for 10 and 60 h were charged to 4.3 V at 0.2 C and discharged at different C-rates. The normalized discharge capacities of the NCA95 cathodes, characterized by relatively large primary particles, decrease faster with increasing C-rate than those of the NCMo95 cathodes (Fig. 3e and Fig. S12, ESI†). More importantly, fast charging is a key requirement for EVs. While the NCA95 cathodes quickly lose capacity with increasing charge rate (capacity loss increases with increasing primary particle size), cells featuring NCMo95 cathodes maintain $>$ 90% of their 0.2 C capacity even at 5 C; at this rate, cells reach full charge in only 12 min (Fig. 3f). The beneficial effect of Mo doping is observed in $Li[Ni_{0.90}Co_{0.10}]O_2$ and $Li[Ni_{0.84}Co_{0.16}]O_2$ cathodes. In addition, the Mo doping similarly improved the cycling stability of $Li[Ni_{0.95}Co_{0.04}Al_{0.01}]O_2$ (NCA95) and $Li[Ni_{0.95}Co_{0.03}Mn_{0.02}]O_2$ (NCM95), confirming that Mo doping improves all classes of Ni-rich layered cathodes with a wide range of compositions (Fig. S13 and S14, ESI†).

To visually demonstrate the effectiveness of particle size refinement in arresting microcrack propagation, cross-sections of NCA95 and NCMo95 cathodes subjected to different lithiation times and charged to 4.3 V were examined (Fig. 4a–c). Even after the first charge, wide microcracks are observed to be emanating from the NCA95 cathode particle core. The microcracks extend to the surface, creating channels for electrolyte infiltration. The degree of microcracking becomes increasingly severe with increasing lithiation time of the cathode. Charged NCA95 particles, lithiated for 60 h, are severely damaged, and their mechanical integrity is irreversibly compromised as the large primary particles are unable to prevent crack propagation. In comparison, the microcracks in charged NCMo95 cathode particles are narrow and cease before reaching the particle surface. Even in the case of NCMo95 cathode particles lithiated for 60 h, the primary particles are small enough to effectively deflect crack propagation and confine the microcracks to the particle interior. The degree of microcracking was estimated by measuring the areal fraction of the microcracks using image analysis software, and plotted as a function of primary particle width (Fig. 4d). The plot clearly reveals the effectiveness of particle size refinement in suppressing microcracking. The repeated opening and closure of microcracks during cycling (Fig. S15, ESI†) enables the formation of impurity layers on crack faces owing to electrolyte attack and increases the charge transfer resistance, R_{ct}, of the cathode. Consistent with the degree of microcracking, the R_{ct} of an NCA95 cathode lithiated for 60 h, based on an impedance spectroscopy analysis,

Open Access Article. Published on 16 November 2021. Downloaded on 5/26/2026 9:29:26 AM.
This article is licensed under a Creative Commons Attribution-NonCommercial 3.0 Unported Licence.

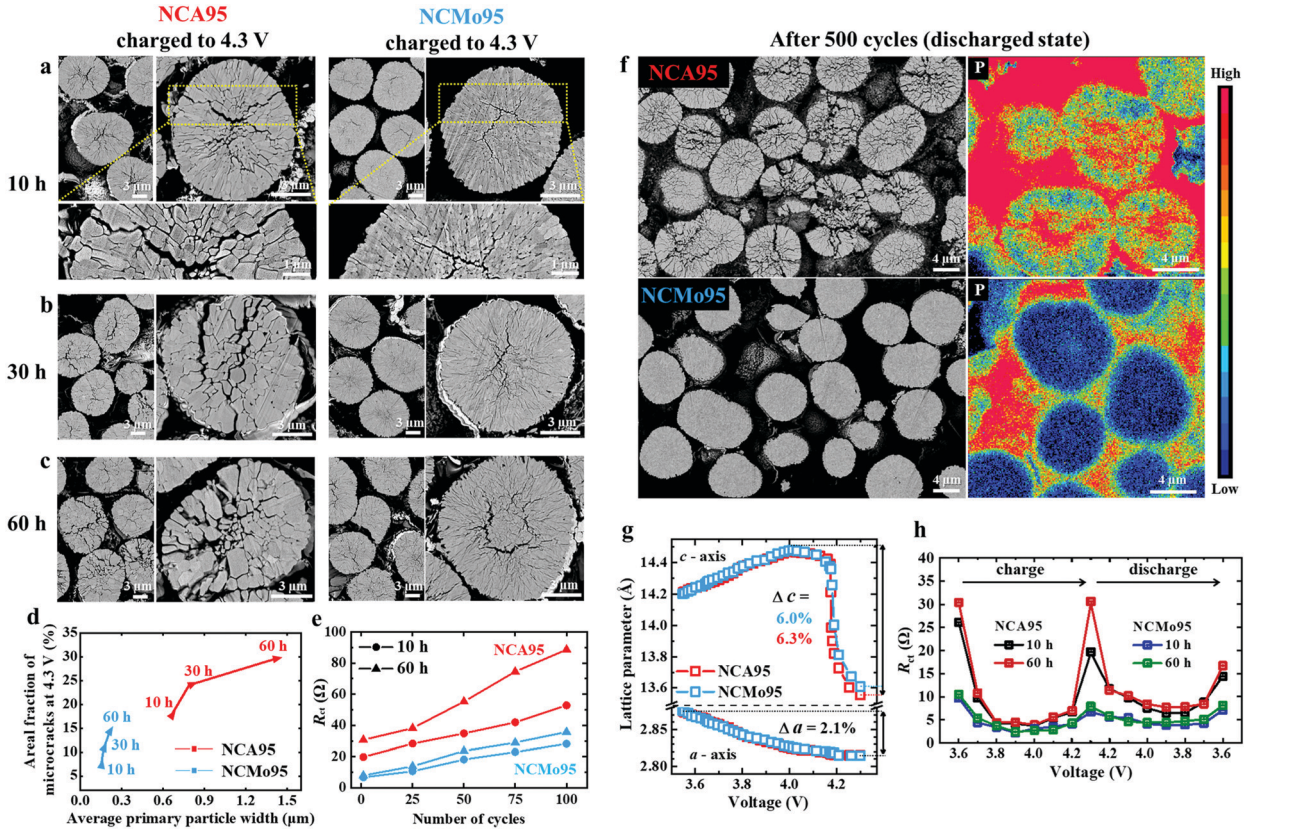

Fig. 4 Fracture durability of NCA95 and NCMo95 cathodes subjected to different lithiation times. Comparison of cross-sectional SEM images of cathodes charged to 4.3 V after the first charge, NCA95 and NCMo95 cathodes lithiated at 700 °C for (a) 10, (b) 30, and (c) 60 h. (d) Areal fraction of microcracks in NCA95 and NCMo95 cathodes calculated from the cross-sectional SEM images. (e) Charge transfer resistance (R_{ct}) of NCA95 and NCMo95 cathodes as a function of cycle number; measured every 25 cycles. (f) Cross-sectional SEM images (left) after 500 cycles in full-cells together with WDS elemental maps of P (right) for NCA95 and NCMo95 cathodes lithiated at 700 °C for 10 h. (g) Comparison of the lattice parameter changes in NCA95 and NCMo95 cathodes lithiated at 700 °C for 10 h. (h) R_{ct} as a function of cell voltage during the cycling of half-cells featuring NCA95 and NCMo95 cathodes subjected to different lithiation times.

increases sharply during cycling, whereas that of an NCMo95 cathode remains relatively low as the electrolyte penetration is minimal (Fig. 4e and Fig. S16, ESI†). Furthermore, cross-sections of NCA95 and NCMo95 cathodes after 500 cycles were examined in their discharged states. As expected, based on the severe capacity fading observed in a cell featuring NCA95 cathode, a substantial fraction of the NCA95 cathode particles are nearly pulverized, and the wavelength-dispersive X-ray spectroscopy (WDS) mapping of P confirms the extensive presence of electrolyte within the cathode particle interiors. In contrast, the cycled NCMo95 cathode displays negligible visible mechanical damage, and corresponding P maps show that the presence of P within the cathode particles is minimal (Fig. 4f). To verify that the superior cycling stability achieved by the NCMo95 cathode stems from particle size refinement rather than from chemical effects associated with the introduction of Mo ions, the dimensional changes of the unit cells of NCA95 and NCMo95 cathodes (lithiated for 10 h) during charging were evaluated by *in situ* XRD. The *c*- and *a*-axis lattice parameters calculated as a function of the state of charge indicate that both cathodes undergo similar dimensional changes in both the *a*- and *c*-directions: a steady expansion followed by abrupt contraction at 4.2 V near the onset of the H2 → H3 phase transition. The maximum change in the *c*-direction for the two cathodes is nearly equal (6.3% for NCA95 and 6.0% for NCMo95), while the unit cells of the cathodes contract identically in the *a*-direction (2.1%) (Fig. 4g and Fig. S17, ESI†). Therefore, the intrinsic abrupt volume contraction observed in the NCA95 and NCMo95 cathodes associated with the H2 → H3 phase transition, which results in the nucleation of microcracks, is virtually identical. Thus, the effect of replacing Al with Mo on the structural change of the cathode during delithiation, and hence, on the magnitude of the detrimental internal lattice strain, is minimal. The *in situ* XRD results confirm that the refined primary particles of the NCMo95 cathode effectively dissipate the strain energy and prevent the formation of microcracks, which can be indirectly observed in terms of the R_{ct} measured during the charge and discharge of NCA95 and NCMo95 cathodes (Fig. 4h and Fig. S18, ESI†). The R_{ct} of the cathodes show a similar trend: the R_{ct} peaks near charge end owing to the onset of the H2 → H3 phase transition and decreases during subsequent discharge.

 This journal is © The Royal Society of Chemistry 2021

Open Access Article. Published on 16 November 2021. Downloaded on 5/26/2026 9:29:26 AM.
This article is licensed under a Creative Commons Attribution-NonCommercial 3.0 Unported Licence.

However, the R_{ct} of the NCMo95 cathode is much lower than that of the NCA95 cathode, especially at full charge, because the microcracks are confined to the particle interiors, which minimizes electrolyte infiltration. In the case of the NCA95 cathode with much larger primary particles, the exposed faces of microcracks formed in the delithiated state develop impurity layers owing to parasitic reactions with the electrolyte, thus causing a sharp increase in R_{ct}. The ability of the NCMo95 cathode to suppress microcrack formation and electrolyte infiltration in the charged state is also confirmed by its enhanced thermal stability, relative to that of the NCA95 cathode (Fig. S19, ESI†).

The electrochemical data demonstrate that particle size refinement is an effective way to improve the cycling stability achieved by Ni-rich layered cathodes, thereby extending battery life without compromising energy-density. To further demonstrate the success of this approach, the effects of introducing

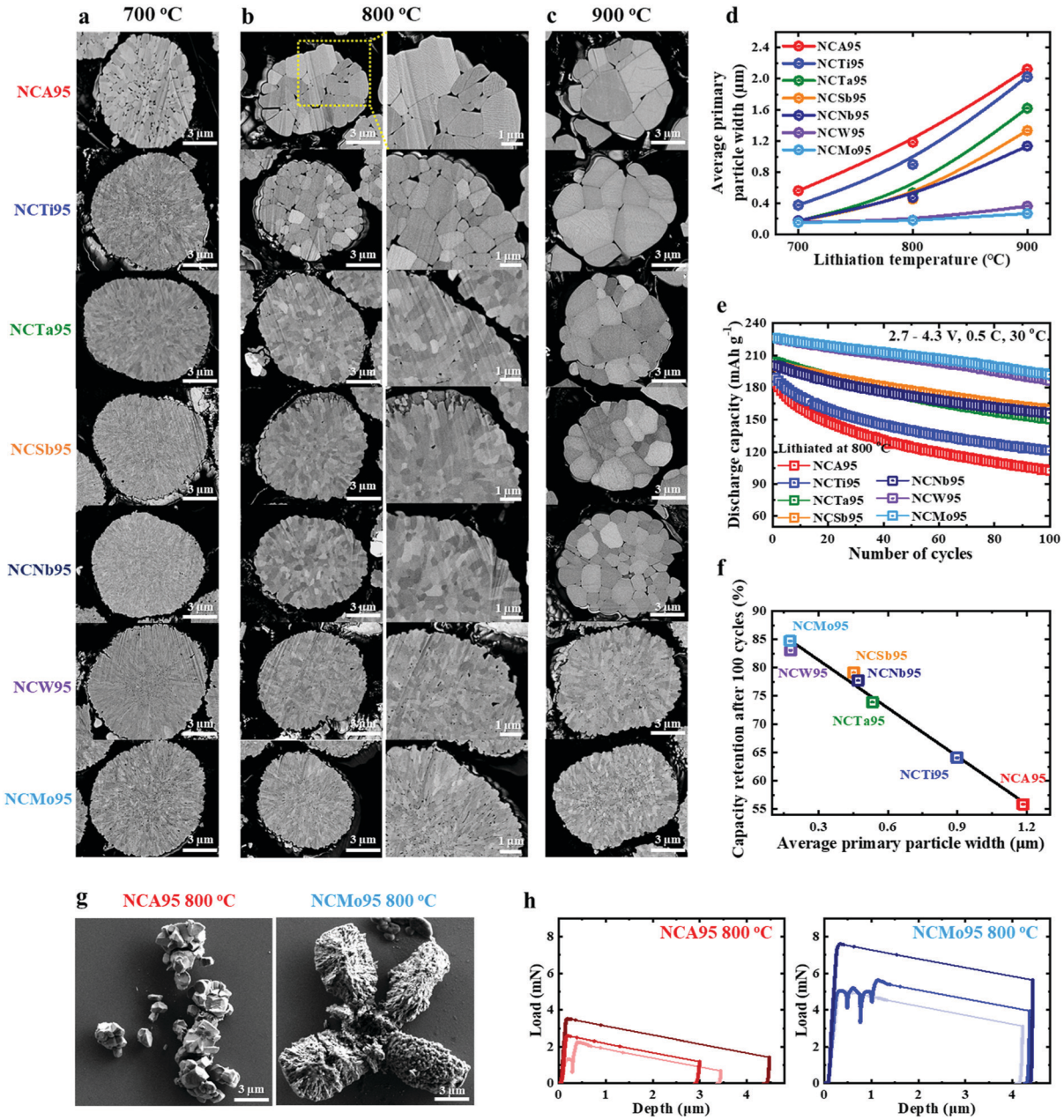

Fig. 5 Comparison of the particle morphologies and electrochemical performances of X-doped (X = Al, Ti, Ta, Nb, Sb, W, and Mo) NC96 cathodes lithiated at various temperatures. Cross-sectional SEM images of NCA95, NCTi95, NCTa95, NCSb95, NCNb95, NCW95, and NCMo95 cathode particles lithiated at (a) 700, (b) 800, and (c) 900 °C for 10 h. (d) Average primary particle width of each cathode as a function of lithiation temperature. (e) Electrochemical cycling performances (at 0.5 C) of cells featuring various cathodes lithiated at 800 °C. (f) Capacity retention after 100 cycles for cells featuring various cathodes lithiated at 800 °C, as a function of average primary particle width, reflecting the relationship between primary particle width and cycle life. (g) Post-compression SEM images of NCA95, and NCMo95 cathode particles lithiated at 800 °C for 10 h. (h) Representative load-displacement curves for NCA95, and NCMo95 cathode particles lithiated at 800 °C for 10 h.

Open Access Article. Published on 16 November 2021. Downloaded on 5/26/2026 9:29:26 AM.
This article is licensed under a Creative Commons Attribution-NonCommercial 3.0 Unported Licence.

different elements into an NC96 cathode on its primary particle size and cycling stability were investigated. The SEM images of NCA95, NCTi95, NCTa95, NCSb95, NCNb95, NCW95, and NCMo95 cathodes lithiated at different temperatures for 10 h display very different primary particle morphologies, despite their respective dopant amounts being equal (1 mol%) (Fig. 5a–c and Fig. S20–22, ESI†). NCA95 cathode particles experience the largest primary particle growth with increasing lithiation temperature while NCMo95 cathode particles experience the least primary particle growth (Fig. 5d). Thus, Mo doping is an effective growth inhibitor that widens the processing temperature in addition to reducing the primary particle width. The primary particle width of the cathodes is unequivocally correlated with cycling stability (Fig. 5e). The NCMo95 cathode achieves the greatest capacity retention after 100 cycles of 85%, followed by the NCW95 (83%), NCSb95 (79%), NCNb95 (78%), NCTa95 (74%), NCTi95 (64%), and NCA95 (56%) cathodes; the decreasing capacity retention corresponds to increasing primary particles width. In fact, an approximately linear relationship between primary particle width and capacity retention is observed (Fig. 5f), strongly suggesting that the chemistry of the dopant has a relatively small effect on cycling stability, which is largely governed by the mechanical toughness of the cathode. To explicitly demonstrate the effect of decreasing the primary particle to a submicrometer scale (< 500 nm), the NCA95 and NCMo95 particles were compressed individually using a flat punch indenter. The post-compression SEM images show that the NCA95 particle fragmented into small pieces of individual or aggregates of primary particles while the NCMo95 particle fractured into large pieces (Fig. 5g). The NCA95 particles were found to have a critical compressive load of 4.0 ± 2.1 mN, after which the particle deforms irreversibly. This corresponds to an estimated yield strength of $\sim 63 \pm 33$ MPa, when normalized by the particle cross-sectional area. The NCMo95 particles had a higher critical load of 5.1 ± 1.6 mN ($\sim 85 \pm 29$ MPa yield strength). This confirms that the nanostructured NCMo95 cathode is stronger under an external stress, even in the absence of electrochemical effects. Although the majority of particles failed rapidly and catastrophically, 3 out of the 18 NCMo95 cathode particles exhibited gradual, serrated flow after the critical load, which indicates a possible higher fracture toughness (Fig. 5h and Fig. S23, ESI†). None of the NCA95 particles showed this level of ductility, although several particles showed multiple yielding events at progressively higher loads. The compression test suggest that fracture toughening is achieved through nanostructured primary particles which helped to dissipate the inherent high mechanical strain accompanying the structural transition near charge end.

Conclusions

The development of high energy-density Ni-enriched layered cathodes (Ni content $> 90\%$) has remained elusive because of the inability of the cathodes to maintain their initial discharge capacity for more than a few tens of cycles. The fast capacity fading of Ni-rich layered cathodes precludes their application in EVs, which typically require batteries that retain 80% of their initial capacity after 500 cycles. Here, it was demonstrated that the limitation of the primary particle size to a submicrometer scale substantially improves the cycling stability achieved by an NC96 cathode. Particle size refinement, achieved by inhibiting the grain growth during lithiation through the introduction of a high-valence dopant, imparts the necessary mechanical toughness to counter the high internal strain associated with the phase transition near charge end. The inhibition of particle growth by Mo doping also widens the processing window for lithiation because the NCMo95 cathode undergoes minimal growth during lithiation. The NCMo95 cathode, whose microstructure is engineered to mitigate the mechanical instability of Ni-rich layered cathodes, represents a next-generation, high energy-density cathode with a long cycle life and fast charging capability. In addition, the NCMo95 cathode has a material cost advantage over current commercial cathodes since Co, a relatively expensive and increasingly scarce resource, is replaced with Ni without compromising battery capacity and battery life.

Experimental

Synthesis of spherical Ni-rich cathode particles

This section describes the synthesis of spherical NCA95, NCTi95, NCTa95, NCSb95, NCNb95, NCW95, and NCMo95 cathode particles ($Li[Ni_{0.95}Co_{0.04}Al_{0.01}]O_2$, $Li[Ni_{0.95}Co_{0.04}Ti_{0.01}]O_2$, $Li[Ni_{0.95}Co_{0.04}Ta_{0.01}]O_2$, $Li[Ni_{0.95}Co_{0.04}Sb_{0.01}]O_2$, $Li[Ni_{0.95}Co_{0.04}Nb_{0.01}]O_2$, $Li[Ni_{0.95}Co_{0.04}W_{0.01}]O_2$, and $Li[Ni_{0.95}Co_{0.04}Mo_{0.01}]O_2$, respectively). A $[Ni_{0.96}Co_{0.04}](OH)_2$ precursor was synthesized through coprecipitation in a batch-type reactor (47 L). An aqueous solution of 2.0 M $NiSO_4{\cdot}6H_2O$ (Samchun Chemicals, 98.5%) and $CoSO_4{\cdot}7H_2O$ (Daejung Chemicals, 98%) (Ni : Co molar ratio = 96 : 4) was prepared as the starting material. This aqueous metal sulfate solution was pumped into a reactor containing a solution of deionized water, NaOH (aq.) (Samchun Chemicals), and NH_4OH (aq.) (Junsei Chemical) under a replenished N_2 atmosphere. Concurrently, 10.5 M NH_4OH (aq.) (NH_4OH to TM = 1.2) and 4.0 M NaOH (aq.) (molar ratio of NaOH to TM = 2.0) were separately pumped into the reactor. The obtained hydroxide precipitate was washed, filtered, and dried at 110 °C. To obtain each cathode material, $[Ni_{0.96}Co_{0.04}](OH)_2$ was mixed with $LiOH{\cdot}H_2O$ (Sigma-Aldrich), and $[Ni_{0.96}Co_{0.04}](OH)_2$ and $LiOH{\cdot}H_2O$ were alternately mixed with $Al(OH)_3{\cdot}3H_2O$, TiO_2, Ta_2O_5, Sb_2O_5, Nb_2O_5, WO_3, and MoO_3 (Sigma-Aldrich) to achieve a Li : (Ni + Co) : X molar ratio of $1.01 : 1–x : x$, where $x = 0.01$ for the doped cathode materials (X = Al, Ti, Ta, Sb, Nb, W, and Mo). Based on the preliminary electrochemical cycling data (initial discharge capacity and cycling stability), 1 mol% is chosen as the optimal dopant content (Fig. S24, ESI†). The mixed powders were calcined in a tube furnace (Lindberg, ThermoFisher) at various temperatures (700, 750, 800, and 900 °C) for various lithiation time (10, 20, 30, and 60 h) under an O_2 atmosphere (heating and cooling rate: 2 °C min^{-1}).

Open Access Article. Published on 16 November 2021. Downloaded on 5/26/2026 9:29:26 AM.
This article is licensed under a Creative Commons Attribution-NonCommercial 3.0 Unported Licence.

Analytical approach

The chemical compositions of the cathode powders were determined by inductively coupled plasma–optical emission spectrometry (ICP-OES, Optima 8300, PerkinElmer). The particle morphologies and cross-sections were observed by scanning electron microscope (SEM, Verios G4UC, FEI). The cross-sections of the powders and electrodes were prepared using a cross-sectional polisher (IB-19520CCP, JEOL). The length, width and aspect ratio of the primary particles and the areal fraction of the microcracks formed within the cathode particles were determined using ImageJ software.[40] The measured length and width of the primary particle correspond to the longitudinal axis and the perpendicular line of a single primary particle, respectively. XRD was performed, using a diffractometer (Empyrean, PANalytical) equipped with a Cu Kα radiation source, to confirm the crystal structures of the cathode materials. XRD data were obtained within the 2θ range of 10–130° at steps of 0.02°. The collected XRD spectra were analyzed using the Rietveld refinement program FullProf. *In situ* XRD analyses were performed in transmission mode using pouch-type cells. The assembled pouch-type cells were charged to 4.3 V by applying a constant current of 0.05 C (9 mA g^{-1}). Concurrently, XRD patterns were recorded every 40 min using a detector (PIXcel 1D, PANalytical). The particle morphologies and crystal structures of the cathodes, and elemental distributions of the dopants were analyzed using a transmission electron microscope (Cs-corrected TEM with Cold FEG, JEM ARM200F JEOL, and Talos F200X, FEI). For differential scanning calorimetry (DSC) measurements, half-cells featuring cathodes charged to 4.3 V were disassembled in an Ar-filled glove box. The obtained electrodes were then thoroughly rinsed with dimethyl carbonate (DMC), and the dried cathode materials were scratched off the current collector. A high-pressure stainless-steel pan sealed with a gold-plated copper seal was used to hold 7.5 mg of a sample and 100 μL of fresh electrolyte (1.2 M $LiPF_6$ in a mixture of ethylene carbonate (EC) and ethyl methyl carbonate (EMC) (EC : EMC volume ratio = 3 : 7) containing 2 wt% vinylene carbonate (VC)). The measurements were performed using a differential scanning calorimeter (DSC 214 Polyma, Netzsch) at a heating rate of 5 °C min^{-1}. Nanoindentation tests were performed using the iMicro nanoindenter (KLA Tencor) and a flat punch of 55 microns in size. The particles were diluted in anhydrous ethanol and then redispersed on silicon wafers. 18 to 20 particles were compressed and unloaded in the nanoindenter at a constant displacement rate of 10 nm s^{-1} and 100 nm s^{-1}, respectively, and data was acquired at 400 Hz. The data was corrected for spring stiffness, nanoindenter frame stiffness, and compliance of the silicon substrate and diamond tip.

Electrochemical tests

For the electrochemical half-cell tests, 90 wt% of a cathode material, 5.5 wt% of a conducting agent (carbon black, Alfa Aeser), 4.5 wt% of poly(vinylidene fluoride) (Solef5130, Solvay), and *N*-methyl pyrrolidone were mixed using a mixer (ARE310, Thinky). Electrodes with an active material mass loading of 4–5 mg cm^{-2} were prepared by coating Al foils (UACJ) with the obtained cathode material slurries, that were then vacuum dried at 110 °C, roll-pressed, and punched into disks with a diameter of 14 mm. Microporous polypropylene/polyethylene/polypropylene (PP/PE/PP) (Celgard 2320, Celgard) and Li-metal (Honjo Metal) served as separators and anodes, respectively. A mixture of EC and EMC (EC : EMC volume ratio = 3 : 7) containing 1.2 M $LiPF_6$ and 2 wt% VC (Panax Etec) served as the electrolyte. CR2032 coin-type (Hohsen) half-cells were fabricated in an Ar-filled glove box. The cells were charged and discharged at a constant current density of 0.1 C (18 mA g^{-1}) and 0.2 C (36 mA g^{-1}), respectively, within a voltage range of 2.7–4.3 V *vs.* Li^+/Li at 30 °C during the first two cycles. The cells were then cycled at a constant current density of 90 mA g^{-1} (0.5 C). The discharge and charge rate capabilities were tested by discharging and charging cells, respectively, according to a galvanostatic profile with systematically increasing current density (18 (0.1 C)–36 (0.2 C)–90 (0.5 C)–180 (1 C)–360 (2 C)–900 (5 C)–1800 (10 C) mA g^{-1}) by fixing the current density as 0.2 C for the other. Long-term cycling stability was tested using a laminated pouch-type full-cell (55 mA h). To fabricate cathodes with an active material mass loading of 9–10 mg cm^{-2} for the full-cells, Al foils were coated with slurries consisting of synthesized cathode materials, carbon black, and poly(vinylidene fluoride) (at a weight ratio of 94 : 3 : 3) in *N*-methylpyrrolidone. Commercial artificial graphite (Posco Chemical) was used for anodes. The sizes of the cathodes and anodes used in the pouch cells were 3 × 5 and 3.1 × 5.1 cm^2, respectively. Based on areal capacity, the full-cell capacity balance (capacity ratio of the negative to positive electrode, N : P ratio) was within the range of 1.15–1.20. The full-cells were cycled between 3.0 and 4.2 V at constant currents of 0.8 and 1 C during charge and discharge, respectively (44 and 55 mA, respectively, corresponding to 200 mA g^{-1}) at 25 °C. Electrochemical impedance spectroscopy (EIS) was conducted using a VMP3 multichannel potentiostat (Bio-Logic) over a frequency range of 1.0 mHz to 1.0 MHz with a voltage amplitude of 10 mV. The charge transfer resistance (R_{ct}) was obtained by fitting the corresponding Nyquist plots using Z-view software.

Author contributions

G.-T. P. and Y.-K. S. conceived and designed the research. G.-T. P., D. R. Y., U.-H. K. and B. N. performed the experiments and characterization of materials. G.-T. P., C. S. Y. and Y.-K. S. analyzed the data. J. L., M. M. W., A. C. L., and X. W. G. performed the nanoindentation tests. G.-T. P., X. W. G., W. C. C., C. S. Y. and Y.-K. S. contributed to the discussion of the results. C. S. Y. and Y.-K. S. wrote the manuscript. All the authors commented on and revised the manuscript.

Conflicts of interest

The authors declare no competing interests.

Open Access Article. Published on 16 November 2021. Downloaded on 5/26/2026 9:29:26 AM.
This article is licensed under a Creative Commons Attribution-NonCommercial 3.0 Unported Licence.

Acknowledgements

This work was supported by a National Research Foundation of Korea (NRF) grant funded by the Korea Government Ministry of Education and Science Technology (MEST) (No. NRF-2018 R1A2B3008794). This work was also supported by the Human Resources Development Program (No. 20184010201720) of the Korea Institute of Energy Technology Evaluation and Planning funded by the Ministry of Trade, Industry and Energy of the Korean Government.

Notes and references

1 B. D. McCloskey, *J. Phys. Chem. Lett.*, 2015, **6**, 3592–3593.
2 H. Budde-Meiwes, J. Drillkens, B. Lunz, J. Muennix, S. Rothgang, J. Kowal and D. U. Sauer, *Proc. Inst. Mech. Eng. D: J. Automob. Eng.*, 2013, **227**, 761–776.
3 *2020 Annual Merit Review, Vehicle Technologies Office* (US Department of Energy, 2020); https://www.energy.gov/sites/prod/files/2020/06/f75/bat317_liu_2020_o_4.22.20_148PM_LR.pdf.
4 K. B. Naceur, Tracking Clean Energy Progress (International Energy Agency, 2016).
5 H.-H. Ryu, K.-J. Park, C. S. Yoon and Y.-K. Sun, *Chem. Mater.*, 2018, **30**, 1155–1163.
6 G. W. Nam, N.-Y. Park, K.-J. Park, J. Yang, J. Liu, C. S. Yoon and Y.-K. Sun, *ACS Energy Lett.*, 2019, **4**, 2995–3001.
7 J.-H. Kim, H.-H. Ryu, S. J. Kim, C. S. Yoon and Y.-K. Sun, *ACS Appl. Mater. Interfaces*, 2019, **11**, 30936–30942.
8 P. Yan, J. Zheng, M. Gu, J. Xiao, J.-G. Zhang and C.-M. Wang, *Nat. Commun.*, 2017, **8**, 14101.
9 K. Du, H. Xie, G. Hu, Z. Peng, Y. Cao and F. Yu, *ACS Appl. Mater. Interfaces*, 2016, **8**, 17713–17720.
10 E. Zhao, M. Chen, Z. Hu, D. Chen, L. Yang and X. Xiao, *J. Power Sources*, 2017, **343**, 345–353.
11 B. Han, B. Key, S. H. Lapidus, J. C. Garcia, H. Iddir, J. T. Vaughey and F. Dogan, *ACS Appl. Mater. Interfaces*, 2017, **9**, 41291–41302.
12 S. Chen, T. He, Y. Su, Y. Lu, L. Bao, L. Chen, Q. Zhang, J. Wang, R. Chen and F. Wu, *ACS Appl. Mater. Interfaces*, 2017, **9**, 29732–29743.
13 H. Yang, H.-H. Wu, M. Ge, L. Li, Y. Yuan, Q. Yao, J. Chen, L. Xia, J. Zheng, Z. Chen, J. Duan, K. Kisslinger, X. C. Zheng, W.-K. Lee, Q. Zhang and J. Lu, *Adv. Funct. Mater.*, 2019, **29**, 1808825.
14 X. Cheng, J. Zheng, J. Lu, Y. Li, P. Yan and Y. Zhang, *Nano Energy*, 2019, **62**, 30–37.
15 B. K. Kim, G. H. Ha and D. W. Lee, *J. Mater. Process. Technol.*, 1997, **63**, 317–321.
16 T. Karthik and S. Asthana, *Mater. Lett.*, 2017, **190**, 273–275.
17 J. Poetschke, V. Richter and R. Holke, *Int. J. Refract. Met. Hard Mater.*, 2012, **31**, 218–223.
18 I. A. Ovid'ko, *Philos. Trans. R. Soc., A*, 2015, **373**, 20140129.
19 K.-J. Park, J.-Y. Hwang, H.-H. Ryu, F. Maglia, S.-J. Kim, P. Lamp, C. S. Yoon and Y.-K. Sun, *ACS Energy Lett.*, 2019, **4**, 1394–1400.
20 H.-H. Sun, J. A. Weeks, A. Heller and C. B. Mullins, *ACS Appl. Energy Mater.*, 2019, **2**, 6002–6011.
21 S. H. Jung, U.-H. Kim, J.-H. Kim, S. Jun, C. S. Yoon, Y. S. Jung and Y.-K. Sun, *Adv. Energy Mater.*, 2020, **10**, 1903360.
22 T. Nishimura, M. Mitomo, H. Hirotsuru and M. Kawahara, *J. Mater. Sci. Lett.*, 1995, **14**, 1046–1047.
23 H.-H. Ryu, K.-J. Park, D. R. Yoon, A. Aishova, C. S. Yoon and Y.-K. Sun, *Adv. Energy Mater.*, 2019, **9**, 1902698.
24 U.-H. Kim, N.-Y. Park, G.-T. Park, H. Kim, C. S. Yoon and Y.-K. Sun, *Energy Storage Mater.*, 2020, **33**, 399–407.
25 X. Wang, Z. Z. Fang and H. Y. Sohn, *Int. J. Refract. Met. Hard Mater.*, 2008, **26**, 232–241.
26 W. Dong, S. Zhu, Y. Wang and T. Bai, *Int. J. Refract. Met. Hard Mater.*, 2014, **45**, 223–229.
27 J. E. Burke and D. Turnbull, *Prog. Met. Phys.*, 1952, **3**, 220–244.
28 J. E. Burke, *J. Am. Ceram. Soc.*, 1957, **40**, 80–85.
29 S. L. Dai, J.-P. Delplanque and E. J. Lavernia, *J. Mater. Res.*, 1999, **14**, 2814–2823.
30 S. H. Brodhag and M. Herwegh, *Contrib. Mineral. Petrol.*, 2010, **160**, 219–238.
31 G.-T. Park, H.-H. Ryu, N.-Y. Park, C. S. Yoon and Y.-K. Sun, *J. Power Sources*, 2019, **442**, 227242–227250.
32 A. Aishova, G.-T. Park, C. S. Yoon and Y.-K. Sun, *Adv. Energy Mater.*, 2020, **10**, 1903179.
33 Y. S. Meng, G. Ceder, C. P. Grey, W.-S. Yoon, M. Jiang, J. Bréger and Y. Shao-Horn, *Chem. Mater.*, 2005, **17**, 2386–2394.
34 C. S. Yoon, M.-J. Choi, D.-W. Jun, Q. Zhang, P. Kaghazchi, K.-H. Kim and Y.-K. Sun, *Chem. Mater.*, 2018, **30**, 1808–1814.
35 U.-H. Kim, J.-H. Kim, J.-Y. Hwang, H.-H. Ryu, C. S. Yoon and Y.-K. Sun, *Mater. Today*, 2019, **23**, 26–36.
36 U.-H. Kim, G.-T. Park, B.-K. Son, G. W. Nam, J. Liu, L.-Y. Kuo, P. Kaghazchi, C. S. Yoon and Y.-K. Sun, *Nat. Energy*, 2020, **5**, 860–869.
37 X. He, P. Ling, J. Qiu, M. Yu, X. Zhang, C. Yu and M. Zheng, *J. Power Sources*, 2013, **240**, 109–113.
38 S. Yang, B. Yan, L. Lu and K. Zeng, *RSC Adv.*, 2016, **6**, 94000–94009.
39 C. Schwab, A. Höweling, A. Windmüller, J. Gonzalez-Julian, S. Möller, J. R. Binder, S. Uhlenbruck, O. Guillon and M. Martin, *Phys. Chem. Chem. Phys.*, 2019, **21**, 26066–26076.
40 C. T. Rueden, J. Schindelin, M. C. Hiner, B. E. DeZonia, A. E. Walter, E. T. Arena and K. W. Eliceiri, *BMC Bioinf.*, 2017, **18**, 529.

 This journal is © The Royal Society of Chemistry 2021